Spectroscopic Observations of Coronal Rain Formation and Evolution following an X2 Solar Flare

David H. Brooks,[1, 2, *] Jeffrey W. Reep,[3] Ignacio Ugarte-Urra,[3] John E. Unverferth,[4] and Harry P. Warren[3]

[1]*Department of Physics & Astronomy, George Mason University, 4400 University Drive, Fairfax, VA 22030, USA*

[2]*University College London, Mullard Space Science Laboratory, Holmbury St. Mary, Dorking, Surrey, RH5 6NT, UK*

[3]*Space Science Division, Naval Research Laboratory, Washington, DC 20375, USA*

[4]*National Research Council Research Associate at the US Naval Research Laboratory, Washington, DC 20375, USA*

ABSTRACT

A significant impediment to solving the coronal heating problem is that we currently only observe active region (AR) loops in their cooling phase. Previous studies showed that the evolution of cooling loop densities and apex temperatures are insensitive to the magnitude, duration, and location of energy deposition. Still, potential clues to how energy is released are encoded in the cooling phase properties. The appearance of coronal rain, one of the most spectacular phenomena of the cooling phase, occurs when plasma has cooled below 1 MK, which sets constraints on the heating frequency, for example. Most observations of coronal rain have been made by imaging instruments. Here we report rare Hinode/EUV Imaging Spectrometer (EIS) observations of a loop arcade where coronal rain forms following an X2.1 limb flare. A bifurcation in plasma composition measurements between photospheric at 1.5 MK and coronal at 3.5 MK suggests that we are observing post-flare driven coronal rain. Increases in non-thermal velocities and densities with decreasing temperature (2.7 MK to 0.6 MK) suggest that we are observing the formation and subsequent evolution of the condensations. Doppler velocity measurements imply that a 10% correction of apparent flows in imaging data is reasonable. Emission measure analysis at 0.7 MK shows narrow temperature distributions, indicating coherent behaviour reminiscent of that observed in coronal loops. The space-time resolution limitations of EIS suggest that we are observing the largest features or rain showers. These observations provide insights into the heating rate, source, turbulence, and collective behaviour of coronal rain from observations of the loop cooling phase.

1. INTRODUCTION

Determining the mechanisms that heat the solar corona to high temperatures remains a difficult unsolved problem in solar physics. There is a consensus that the coronal magnetic field is key, however, there is continuing debate on the precise details of how energy is stored and dissipated. Two long standing lines of investigation involve the dissipation of Magnetohydrodynamic (MHD) waves and the reconnection of braided magnetic fields. In the MHD wave heating scenario, turbulent motions in the photosphere lead to the propagation of Alfvén waves along the magnetic field into the corona (van Ballegooijen et al. 2011). In the reconnection scenario, field line braiding leads to the build-up of magnetic stress later released by topological rearrangement (Gold & Hoyle 1960; Parker 1983, 1988). Other agents of energy transfer have been proposed in recent years, such

as chromospheric jets (De Pontieu et al. 2009, 2011) or solar tornadoes (Wedemeyer-Böhm et al. 2012). It seems clear that all these processes occur in the corona, and the challenge is to ascertain which one is dominant in a given structure at a specific time. Recent reviews are given by Klimchuk (2006), Parnell & De Moortel (2012), and Reale (2014).

One way to make progress on this problem is to compare state-of-the-art numerical simulations with the observations, but this has its own difficulties. Current 3-D numerical simulations and observations cannot resolve the small spatial scales involved in the heating process (Shay et al. 2001; Pontin & Priest 2022). Radiation signatures of the process also appear after the mechanism has heated the plasma and we are already observing the cooling phase. This is a significant barrier to further progress. Hydrodynamic simulations suggest that loop densities and apex temperatures do not depend clearly on the magnitude, duration, or location of the energy deposition (Winebarger & Warren 2004). This implies that observations need to be made early in the loop evolution

* Present address: Hinode Group, ISAS/JAXA, 3-1-1 Yoshinodai, Chuo-ku, Sagamihara, Kanagawa 252-5210, Japan

to infer information about the heating parameters. That being said, observations of the cooling phase can be a potential source of information on other aspects of the loop heating and cooling process, and therefore provide useful constraints for numerical models.

One striking observational feature of cooling loops is the appearance of coronal rain (Schrijver 2001). Coronal rain clumps form in coronal loops as condensations due to the onset of a thermal instability when high radiative losses cause catastrophic cooling (Müller et al. 2003). It can be created in numerical hydrodynamic simulations if the heating is concentrated at the loop footpoints (Antiochos et al. 1999; Karpen et al. 2001; Müller et al. 2005). This already tells us something about the heating mechanism, despite only observing the loops cooling, and sets limitations on the process itself since, for example, Alfvén waves generate uniform heating in some models (Antolin et al. 2010), but localize heating to the loop footpoints in others (Downs et al. 2016). Uniform (smooth) temperature distributions tend to inhibit the formation of coronal rain.

The heating frequency also impacts rain formation. High-frequency heating leads to Thermal Non-Equilibrium (TNE) and cyclic heating (evaporation) and cooling (condensation) behavior, manifested as long-period intensity pulsations at high temperatures and coronal rain at lower temperatures (Froment et al. 2015; Antolin 2020). There is some evidence that the occurrence of TNE depends on a relatively narrow set of heating parameters (Froment et al. 2018). Physically, coronal rain can be produced in 3-D radiative MHD simulations due to heating by the Ohmic dissipation of field line braiding as a result of convective motions in the photosphere (Kohutova et al. 2020). This is impulsive heating, and coronal rain has also been observed in solar flares (Jing et al. 2016) and non-flaring dynamic events (Kohutova et al. 2019). The typical short duration non-thermal electron beam heating at loop footpoints in flares, however, does not seem to be able to produce coronal rain (Reep et al. 2020), though note that rain is generated if TNE and beam heating are combined.

Observationally, most studies have focused on chromospheric data where the rain is most visible falling and tracing the paths of the magnetic field. Typical coronal rain velocities are on the order of 30–100 km s^{-1} (Antolin & Rouppe van der Voort 2012; Ahn et al. 2014), with extreme values up to 200 km s^{-1} being reported (Kleint et al. 2014). The widths of coronal rain clumps are 200-300 km on average with minima and maxima in the range of 150–800 km for quiescent rain (Antolin & Rouppe van der Voort 2012), and 120 km for flare-driven

rain (Jing et al. 2016) when observed at high spatial resolution. There is a tendency for the clumps to be wider at higher temperatures, and to show an association with the spatial resolution of the observing instrument (Antolin & Froment 2022).

The temperature evolution of the multi-thermal cooling plasma has been tracked using differential emission measure (DEM) techniques applied to SDO/AIA images (Antolin et al. 2015; Scullion et al. 2016; Kohutova & Verwichte 2016; Froment et al. 2020), and a fairly wide range of density measurements have been inferred indirectly: $\log(n/cm^{-3}) = 10.3$–11.4 from EUV absorption by hydrogen and helium (Antolin et al. 2015), $\log(n/cm^{-3}) = 10.8$–12.0 from an emission measure analysis of Hα data (Froment et al. 2020), and $\log(n/cm^{-3}) = 11.9$ from combining a volume estimate with a DEM measurement in flare-driven rain (Scullion et al. 2016). For an extensive review of coronal rain and all these properties see Antolin & Froment (2022) and references therein.

There have been no measurements of elemental abundances, though coronal rain associated with impulsive events and flares would suggest the likelihood of a photospheric composition (Warren 2014; Warren et al. 2016). In contrast, coronal rain forming in active region loops ought to show a coronal composition, thus making it easier to form due to the larger radiative losses.

Most of the information we know about coronal rain, and described here, comes from imaging data, chromospheric observations, and modeling, yet the rain features first condense and form in the corona and cool through the transition region where EUV spectroscopic data is, in principal, obtainable by instruments such as the EUV Imaging Spectrometer (EIS, Culhane et al. 2007) on Hinode (Kosugi et al. 2007). One difficulty with using EIS is that the transition region emission lines are weak. Another issue is that coronal rain is most readily observed off-limb, and the main aim of Hinode is to combine coronal observations with measurements of the photospheric magnetic field, which necessarily leads to an operational mode that favors on-disk observations and a tendency to make spatial maps.

Nevertheless, on 2023, March 3, spectacular coronal rain was observed following an X2.1 flare in AR 13234. EIS was observing off-limb in sit-and-stare mode, positioned near the apex of a loop system where coronal rain was falling. This allowed us to obtain rare measurements of the formation and evolution of coronal rain. Here we report these new spectroscopic observations, including density, temperature, and plasma composition measurements as the rain first condenses and forms. We also discuss the implications of our measurements.

2. DATA PROCESSING

We use data from the Solar Dynamics Observatory (SDO, Pesnell et al. 2012) Atmospheric Imaging Assembly (AIA, Lemen et al. 2012) in this work. AIA images the Sun at high spatial ($0.6''$ pixels) resolution and high time ($12\,\mathrm{s}$) cadence in a range of filters sensitive to different layers of the solar atmosphere. All of the data shown here were retrieved from the Stanford JSOC (Joint Science Operations Center) and processed with standard calibration procedures available in SolarSoftware (SSW, Freeland & Handy 1998).

Our main emphasis is on the spectroscopic measurements made by the Hinode/EIS. EIS records solar spectra in two wavelength bands from 171–212 Å and 245–291 Å at moderate spatial resolution ($1''$ pixels) and high spectral resolution ($22\,\mathrm{mÅ}$). EIS typically observes in rastering or sit-and-stare mode. In raster mode, the fine mirror is moved to build up a series of slit exposures across an area of the Sun. In sit-and-stare mode, the mirror does not move, and repeated exposures are made at the same position. The selected observing mode is a compromise between spatial coverage and temporal cadence. Typically, sit-and-stare mode is used to observe the evolution of a particular feature at relatively high time cadence. For features such as flares, there is an element of luck in being positioned in the right place at the right time. The data presented here are from a relatively uncommon observation where the EIS slit was well positioned at the top of a limb AR loop arcade.

The observing sequence studied here used the $2''$ slit in sit-and-stare mode, and took a sequence of 80 consecutive exposures. The exposure time for these observations was $40\,\mathrm{s}$, and the resulting cadence was $42\,\mathrm{s}$. An extensive line-list was used, including spectral lines of He II, O V–O VI, Mg V–Mg VII, Si VII, Si X, Al IX, S X, S XIII, Ar XIV, Ca XIV–Ca XVII, Fe VIII–Fe XVII, Fe XXIII, and Fe XXIV. This selection includes several density and elemental abundance diagnostics, and a wide range of lines suitable for measuring the atmospheric temperature structure (differential emission measure). We discuss the specific diagnostics we use in Sect. 3.

The observing sequence was run 4 times on 2023, March 03, from 18:57:34–22:41:16 UT. We processed the level-0 FITS files using the standard eis_prep procedure in SSW. This code removes the dark current pedestal, handles warm, hot, dusty pixels and cosmic ray strikes, and converts the data to physical units by applying the radiometric calibration. For this analysis, we used the absolute calibration of Warren et al. (2014).

The EIS team routinely monitor the pointing relative to AIA full-disk images using wide-slit ($266''$) data. This allows calibration of the EIS-AIA offset. We coaligned the EIS and AIA data taking this offset into account. We also corrected the EIS pointing for the satellite jitter in the X- and Y-directions.

3. DATA ANALYSIS AND OBSERVATIONAL RESULTS

3.1. Overview of activity

Active region NOAA 13234 crossed the solar disk from 2023, February 19 until March 5. Originally classified as a bipolar β sunspot group, it developed a $\beta\gamma\delta$ configuration with continuous flux emergence in the core, and rotational behavior producing shearing around the mixed-polarity trailing δ spot. It was the target of a Max Millenium Major Flare Watch for long periods, and produced multiple flares greater than M-class. An X2.1 event occurred as the region sat on the west limb, peaking at 17:52 UT on 2023, March 3 (SOL2023-03-03) according to the Hinode Flare Catalogue (Watanabe et al. 2012). The flare itself had a fast rise phase but fairly slow decay. EIS started observing about an hour later, and we observed the coronal rain with the sit-and-stare flare mode sequence.

Figure 1 shows multiple AIA images of AR 13234 and the coaligned position of the EIS slit at 21:52:45–21:52:57 UT. The figure is one frame from the animation available in the online manuscript. The animation shows the same image format, and overplots the position of the EIS slit when the sit-and-stare observations are running. Prior to the flare onset, we see quiescent coronal rain falling around the active region in the 304 Å images. Bright condensations appear to form at the loop tops, and these are particularly clear from 16:42 UT. They are seen as falling dark absorption features that are visible in all the other filters except 94 Å. The flare starts at 17:42 UT (Watanabe et al. 2012), and is quickly followed by a bright eruption surrounding another dark absorption feature in the 304 Å images. This feature appears to be an erupting filament, and is also visible in all filters except 94 Å. The erupting loop arcade is very prominent in the animation. This eruption destabilizes the loop arcade, and appears to energize the loop top region where the coronal rain had previously been forming. The system then begins to relax, and similar bright coronal rain (in 304 Å) and dark absorption features (other wavelengths except 94 Å) start to form and fall again. To be clear, quiescent active region coronal rain is falling throughout the period of the flare. There is no break in rain activity due to the flare, though the loops hosting the rain are disrupted by it and temporarily obscured in the animation by the bright flare emis-
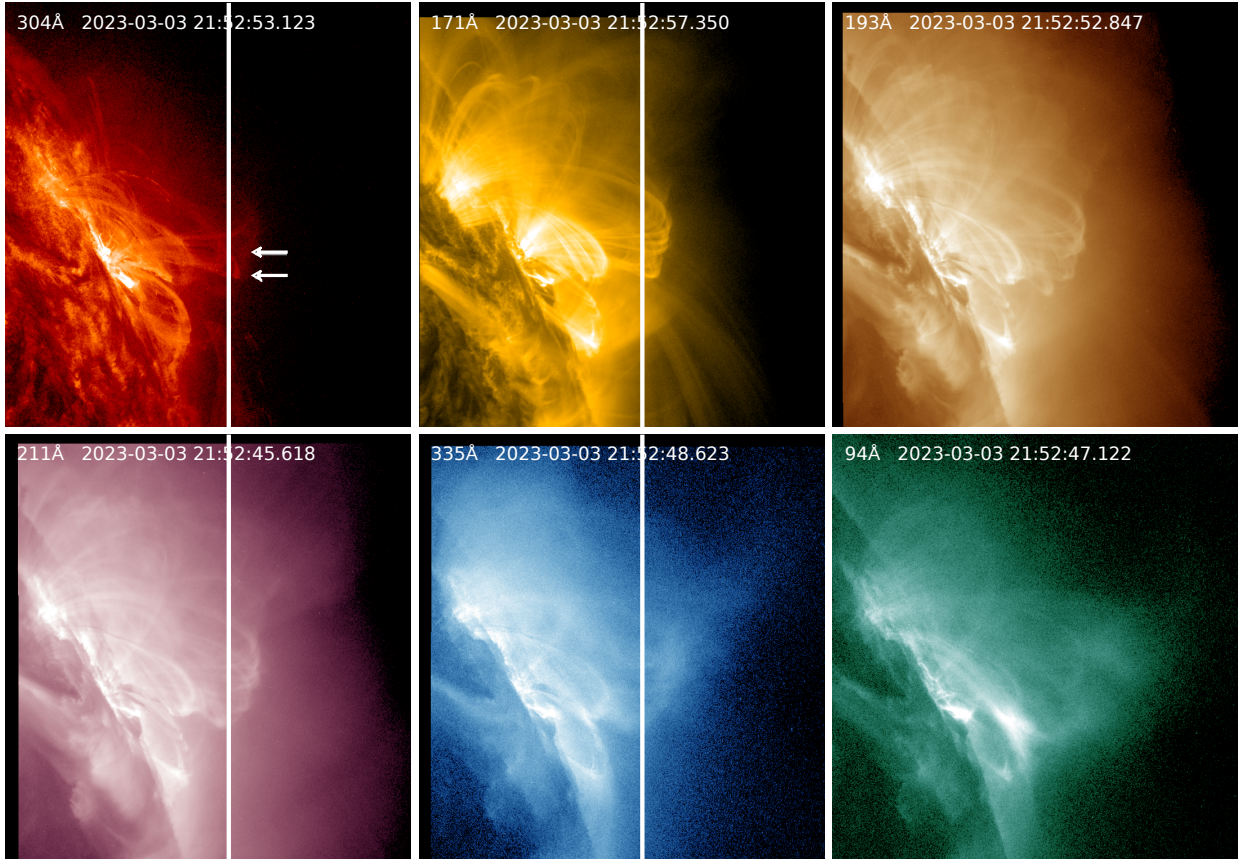
Figure 1. Context images from SDO/AIA showing the loop system in the west limb AR and the location of the EIS slit. An animation showing the time-period of the flare and EIS observations is available in the HTML version of the article. This figure is one frame from the animation, which lasts 12 s and spans the period 16:01:21–22:58:45 UT. The filters and observation times are indicated in the legends. The filters are sensitive to plasma temperatures of 0.09 MK (304Å), 0.8 MK (171Å), 1.4 MK (193Å), 1.8 MK (211Å), 2.5 MK (335Å), and 7.1 MK (94Å) in active regions, respectively, with contributions from continuum and higher temperature lines during flares. We show the EIS slit position with the vertical white line on the AIA images used to coalign with EIS in Figure 2. The arrows on the AIA 304 Å image show the locations that are tracked by the horizontal dashed lines in Figure 2.

sion. As the brightness subsides these loops are visible again and rain is falling.

As EIS begins to observe at 18:57:34 UT, 65 mins after the flare peak, the slit is well positioned close to this coronal rain formation region at the loop tops. It is unclear, however, whether the post-flare rain EIS observes is actually driven by the flare, or whether it is quiescent rain typical of this active region that has restarted once the disruption of the flare is over i.e. rain similar to that which was observed by AIA prior to the flare. This is an important question since these observations could provide new constraints for numerical modeling. Current models fail to adequately reproduce flare-driven rain, since the heating in a flare is so strong that conduction quickly diffuses away any perturbation that can give rise to the growth of a rain clump (Reep et al. 2020). The only way we confidently know how to

produce rain in loop simulations is through thermal non-equilibrium with steady footpoint heating, which seems contradictory to the impulsive flare scenario. Furthermore, there are significant differences in the modeling if the rain forms close to the flare impulsive phase, rather than well into the gradual phase. In our observations, if the rain is flare driven, it is immediately visible close to the impulsive phase. In section 3.4 we use EIS plasma composition measurements to conclude that this rain is indeed flare-driven.

Two positions are pointed out with arrows in the animation of Figure 1. These correspond to the locations of bright tracks seen in the time-distance plots of Figure 2. Figure 2 shows time-distance plots for several AIA filters and EIS spectral lines that correspond to broadly similar formation temperatures. These demonstrate the accuracy of the EIS-AIA coalignment and highlight the fea-
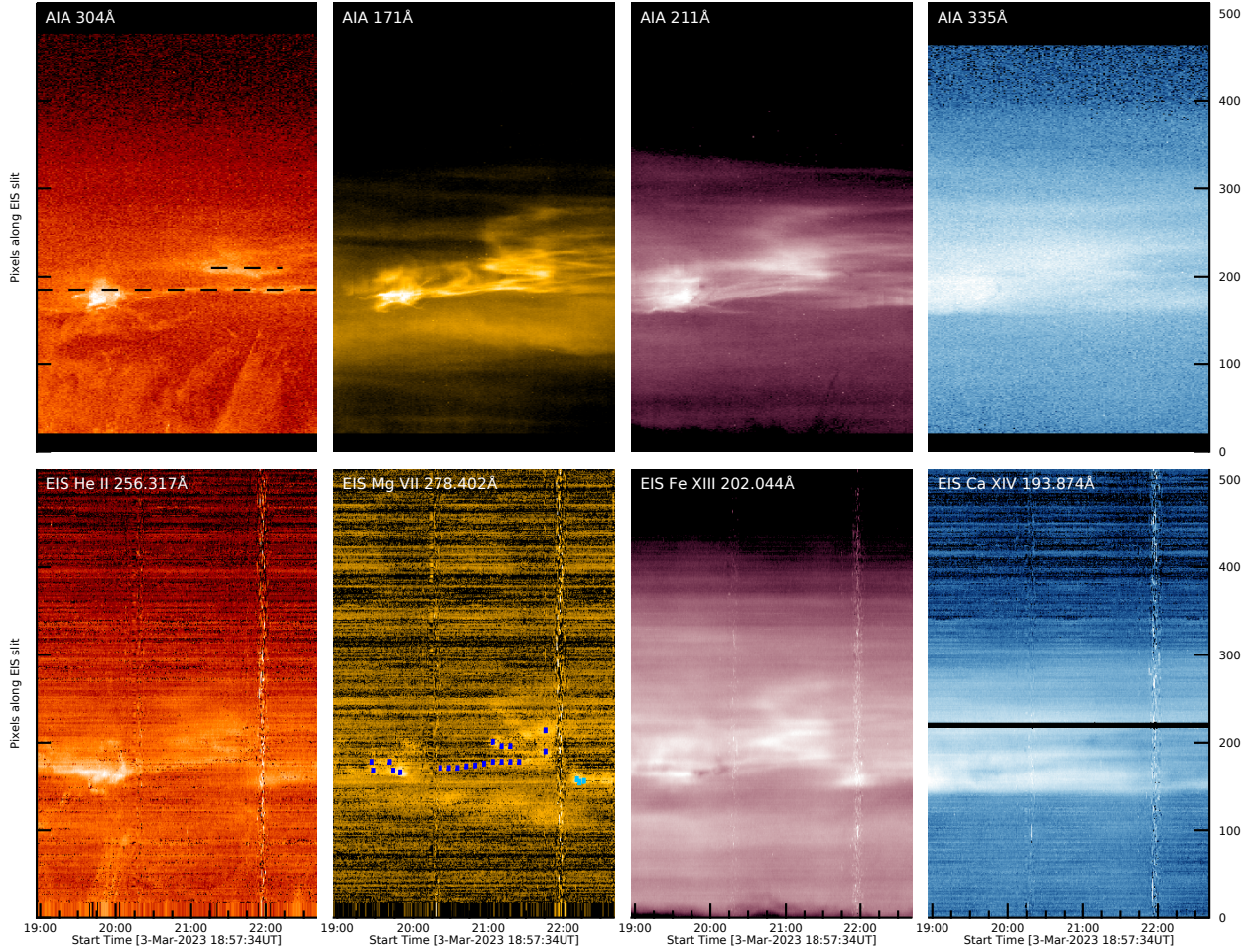
Figure 2. Time-distance plots showing the accuracy of the AIA/EIS coalignment and identifying the features associated with coronal rain and the loop system. Top row: AIA time-distance plots at the position of the EIS slit. Bottom row: EIS time-distance plots. We show the AIA filters and EIS spectral lines used in the legends. The dashed lines on the AIA 304Å image indicate trails produced by the continuous passage of rain features across the EIS slit. The Y-pixel positions corresponding to these trails are highlighted by arrows in the animation for Figure 1. The dark blue boxes show the positions where the spectroscopic diagnostic measurements were made. The light blue boxes show the positions where extra analysis was performed on the Mg data (see text). The horizontal black line in the Ca XIV 193.784 Å image is a result of contamination on the detector.

tures produced by the coronal rain. Looking at the AIA 304 Å and EIS He II 256.317 Å plots we can see a bright feature around Y-pixels 150–200 and 19:30–20:00 UT. This corresponds to the bright loop top blobs of coronal rain that form and cross the EIS slit at the position of the lower arrow in the animation. Rain is crossing here almost throughout the EIS observing period and it produces the horizontal track in the 304 Å time-distance plot (highlighted with the lower dashed-line in Figure 2). Slightly higher and later, around Y-pixel 210 and 21:30–22:00 UT, there is another horizontal trail (highlighted with the upper dashed-line). This corresponds to the weaker material forming and crossing at the position of the upper arrow in the animation. That coronal rain is visible in EIS transition region lines (Mg VI) has

been demonstrated before (Ugarte-Urra et al. 2009), and the coronal rain trails here are clearly visible in the EIS He II 256.317 Å and Mg VII 278.402 Å images, though the morphology is not exactly the same due to the different temperature and instrument sensitivities, the orbital motion of the EIS slit, and the accuracy of the coalignment. The trails in the time-distance plots for the other wavelengths (Fe XIII 202.044 Å and Ca XIV 193.874 Å) indicate that the hotter host loops are being observed at these positions at higher temperatures.

To measure the spectroscopic properties of coronal rain in EIS sit-and-stare observations, we need to ensure sufficient spatio-temporal averaging to obtain a good signal-to-noise (S/N) ratio in the spectrum. Previous studies give guidance on how to approach this prob-
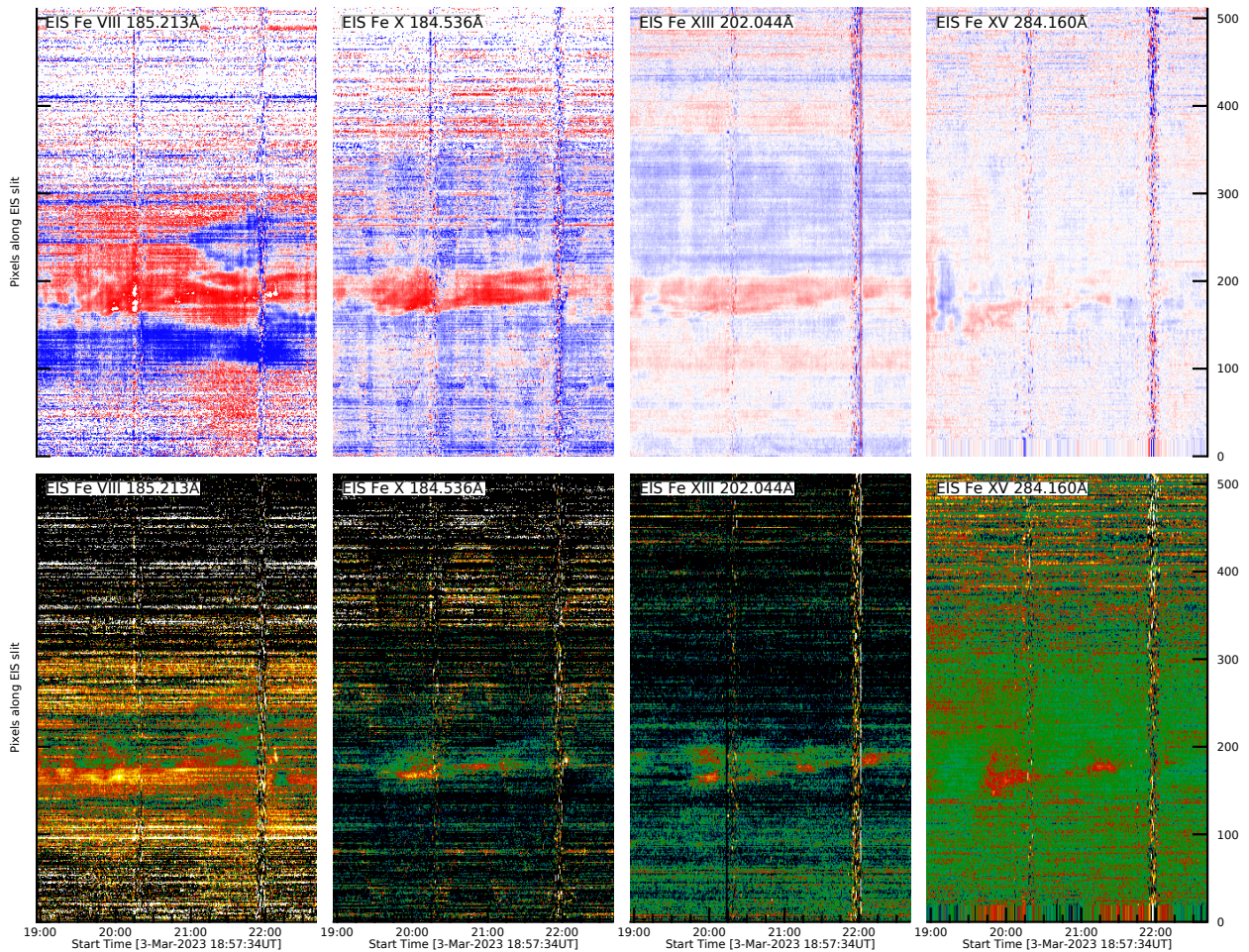
Figure 3. Time-distance plots of Doppler (top row) and non-thermal (bottom row) velocities derived from the EIS data. The spectral lines are indicated in the legends and cover a broad range of theoretical temperatures: 0.5 MK (Fe VIII 185.213 Å), 1.0 MK (Fe X 184.536 Å), 1.7 MK (Fe XIII 202.044 Å), and 2.2 MK (Fe XV 284.160 Å). Blue/red indicates emission moving towards/away from the observer. The Doppler velocity maps are scaled to $\pm$ 25 km s^{1}. The non-thermal velocity maps are scaled from 1–80 km s^{-1} (Fe VIII 185.213 Å and Fe X 184.536 Å) or 1–50 km s^{-1} (Fe XIII 202.044 Å and Fe XV 284.160 Å).

lem. Given the range of widths and velocities quoted in the introduction, a large (300 km) and slow (30 km s^{-1}) clump is still smaller than the 725 km spatial pixels of EIS, and would pass through the 2″ slit location on the order of the exposure time (40 s). It means that in most cases the coronal rain clumps are contained within 1 EIS spatio-temporal pixel, and, unfortunately, this implies that we are not measuring individual clumps in our EIS observations.

Nevertheless, previous observations also show that coronal rain clumps appear to evolve coherently on larger spatial scales of a few Mm (Şahin & Antolin 2022), and this has been referred to as a coronal rain shower. It therefore suggests that although we are likely not measuring the properties of individual clumps of coronal rain, we are making measurements of the largest clumps

or the rain showers, or in fact averages of clumps that are representative of the whole shower or loop envelope. We therefore averaged over the smallest areas possible, consistent with obtaining a good S/N ratio for the spectra. This resulted in box sizes of 3″×5″ (~2.2×3.6 Mm).

The value of the S/N ratio within these boxes, defined here as the ratio of the peak intensity to the background intensity, that is adequate to obtain a good fit to the observed profile depends on the specific spectral line. For the strong Fe VIII–Fe XVI lines, the values fall in the range of 5.8 to 83.5; with the lowest value for Fe IX 197.862 Å and the highest value for Fe XII 195.119 Å. We initially selected 20 boxes in total in the coronal rain trails of the Mg VII 278.402 Å time-distance plot (shown in dark blue in Figure 2). Although the coronal rain is seen most clearly in He II 256.317 Å, all of the EIS
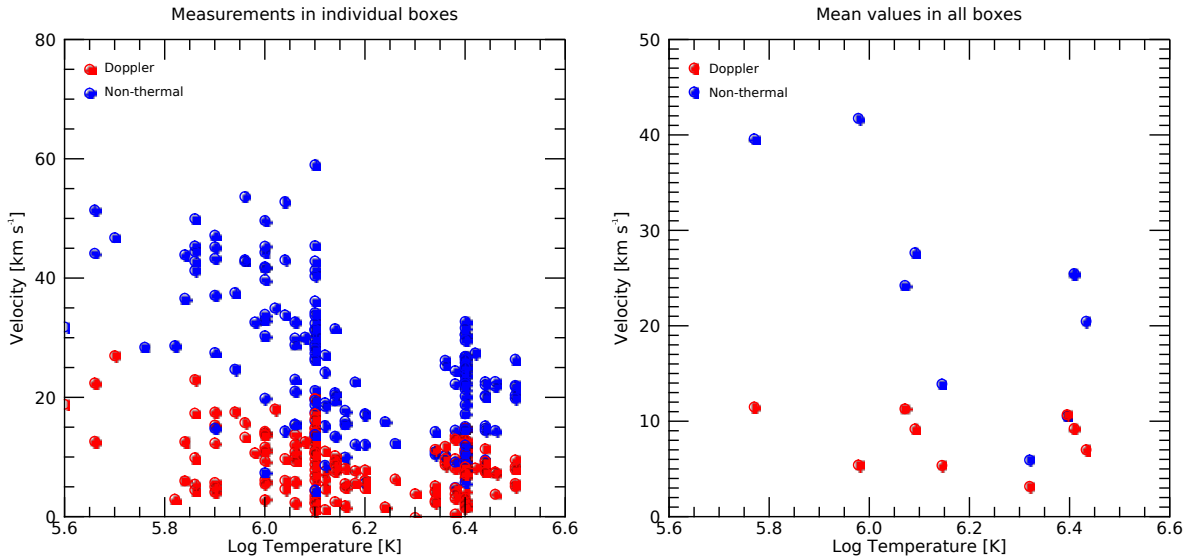
Figure 4. Coronal rain and cooling host loop velocity analysis. Left panel: Doppler (red) and non-thermal (blue) velocities measured in the dark blue boxes of Figure 2 as a function of effective formation temperature. Lines from Fe VIII–Fe XVI were used. Right panel: Mean values of the Doppler (red) and non-thermal (blue) velocities in all the boxes, plotted as a function of the average effective formation temperature.

diagnostics are sensitive to higher temperatures. In particular, the Mg VII 280.737/278.402 diagnostic ratio allows us to measure the density in the coronal rain itself, so we needed to ensure that we chose areas where there is relatively strong emission in these lines. This is why we used Mg VII to identify locations. The other density and composition measurements are made at higher temperatures in the host loops where the rain forms as the loop cools. We confirmed that the boxes we chose were large enough to get a good signal in all the lines analyzed, sometimes with the exception of the weak density diagnostic Mg VII 280.737 Å line. This is discussed further in Section 3.5. Following the conclusions from that section, we selected 3 separate boxes (light blue in Figure 2) to supplement the analysis.

3.2. *Velocities in the host coronal loops*

Figure 3 shows time-distance plots of Doppler and non-thermal velocities derived from several EIS spectral lines spanning the range of temperatures we analysed. Since EIS does not have an absolutely calibrated wavelength scale, these maps show relative Doppler velocities. As with the intensity maps in Figure 2, the spatial offsets between the long- and short-wavelength detectors were corrected using the neural network model of Kamio et al. (2010). The same model was used to adjust for the orbital motion of the spectrum across the detector. This model uses an artificial neural network to establish a relationship between the drift of the spectrum across the

detector and temperature variations inside the instrument due to the changing thermal environment around the satellite orbit. The resultant empirical model reproduces the spectral drift to within $4.4\,\mathrm{km\,s^{-1}}$, and also returns the spectral curvature and spatial offsets. The velocities were also calculated with respect to a reference wavelength where the line-of-sight flows are assumed to average to zero. Typically, for on disk observations, a region of quiet Sun is used, but even there coronal lines are expected to be slightly blue-shifted (Peter 2001). Here, we are observing off-limb, so these blue-shifts are in the radial direction and the average blue-shift along the line-of-sight is expected to be smaller leading to a lower uncertainty and more accurate velocity measurements (Warren et al. 2011). We chose the top 100 pixels of the slit across the whole time-sequence and averaged all the spectra to produce reference wavelengths for each line. The final velocity maps were detrended for residual variations as described in the appendix of Brooks et al. (2020). The non-thermal velocities were calculated following the methods of Brooks & Warren (2016). Briefly, the absolute intensity calibration has a tendency to increase the line widths, so we used the uncalibrated data to calculate the non-thermal velocities. The line widths were also corrected for the instrumental width variation

N-S along the slit using the routine eis_slit_width prepared by Young (2011) [1] and available in SSW.

Fe VIII 185.213 Å is formed closest in temperature to the Mg VII 278.402 Å line where we observe the coronal rain. We see a trail of red-shifted plasma in Fe VIII 185.213 Å (top left panel) where we see a rain related intensity trail in Mg VII 278.402 Å (Figure 2), however, the red-shifts are not co-spatial and cover a more extensive area. The trail of increased non-thermal velocity in Fe VIII 185.213 Å also appears to correspond better with the intensity trail in Mg VII 278.402 Å. This suggests that the Doppler velocity measurements may be picking up emission from the surrounding loops, or that the extent of the coronal rain clumps within the host loop increases as the loop cools. At higher temperatures, we see narrower and weaker red-shift trails, and clumps of enhanced non-thermal velocities. Our actual measurements of the rain and host loop Doppler and non-thermal velocities are, of course, made in the selected boxes.

Figure 4 shows the Doppler and non-thermal velocity measurements obtained from the Fe VIII–Fe XVI lines for the dark blue boxes in Figure 2. To be clear, there are two velocity measurements (Doppler and non-thermal) for each spectral line in each of the 20 boxes. In the left panel, showing all the measurements, the non-thermal velocities increase with decreasing temperature, but there is no obvious trend with temperature in the Doppler velocities. This plot shows a lot of scatter, however, the trends are evident and more clearly seen in the summary plot that shows the average value at each temperature in all the dark blue boxes (right panel). We plot the unsigned Doppler velocities since we are not concerned with the direction of the flows along the line-of-sight, but in any case 90% of the measurements are red-shifted. They fall in the range of 0.1–27 km s^{-1} with a mean value of 8.6 km s^{-1}. This is consistent with the mean Doppler velocity of ∼10 km s^{-1} (also red-shifted) obtained by Antolin & Rouppe van der Voort (2012) from spectropolarimetric data (CRISP, Scharmer et al. 2008) in the chromospheric Hα line. Antolin & Rouppe van der Voort (2012) also found a mean plane-of-sky velocity of ∼65 km s^{-1}, suggesting that a 10% correction for EIS Doppler velocities up to ∼30 km s^{-1} is reasonable. There is no clear trend with temperature. According to previous work, rain clumps show moderate velocities (30–50 km s^{-1}) at the loop top, accelerating to 100–150 km s^{-1} further down the loop leg (Oliver

[1] EIS Software Note No.7, SolarSoftware, $SSW/Hinode/eis/doc/eis_notes

et al. 2014). Our new spectroscopic measurements are smaller at the loop top, and the rain clumps would likely need to cool to chromospheric temperatures before they are accelerated significantly. This suggests that we are observing the rain clumps too early in the formation process to detect any evidence of acceleration while cooling e.g. due to gravity.

The non-thermal velocities fall in the range of 0–59 km s^{-1} with a mean value of 23.3 km s^{-1}. The trend of increasing non-thermal velocity with decreasing temperature shows a strong linear Pearson correlation coefficient of -0.6. There are several possible sources of this non-thermal broadening and assessing their relative contributions benefits from measurements of the electron density. We investigate the densities in the following sections and discuss the implications for the broadening further in Section 3.6.

Inspection of the values within the region covered by the boxes did not reveal any correlation, or obvious temporal delay, between the unsigned Doppler and non-thermal velocities below 1 MK, where we are potentially making measurements in the rain rather than in the host loops. Note that we calculated the non-thermal velocities assuming that the ion temperature is equal to the effective formation temperature i.e. the temperature of the peak of the contribution function convolved with the DEM distribution of the box. We also used that temperature to plot the values.

3.3. *Density and temperature analysis of the host loops*

To compute the DEM within the dark blue boxes we used the Markov-Chain Monte Carlo (MCMC) code available in the PintOfAle software package (Kashyap & Drake 1998, 2000), together with the CHIANTI database (Dere et al. 1997) v.10 (Del Zanna et al. 2021) for all the atomic data. We also assume that the elemental abundances correspond to those of the solar photosphere (Scott et al. 2015b,a). The MCMC algorithm solves the inversion equation

$$I_{ij} = \int G(T,n)\phi(T)dT \qquad (1)$$

by performing a series of reconstructions (100 in our case) that reduce the differences between the calculated and measured spectral line intensities. In Equation 1, I_{ij} is the line intensity for the atomic transition between levels i and j, $\phi(T)$ is the DEM as a function of temperature, T, and $G(T,n)$ is the usual contribution function dependent on temperature and density, n. To reduce the problem to a temperature inversion, we also measure the electron density using the Fe XIII 202.044/203.826 diagnostic ratio.
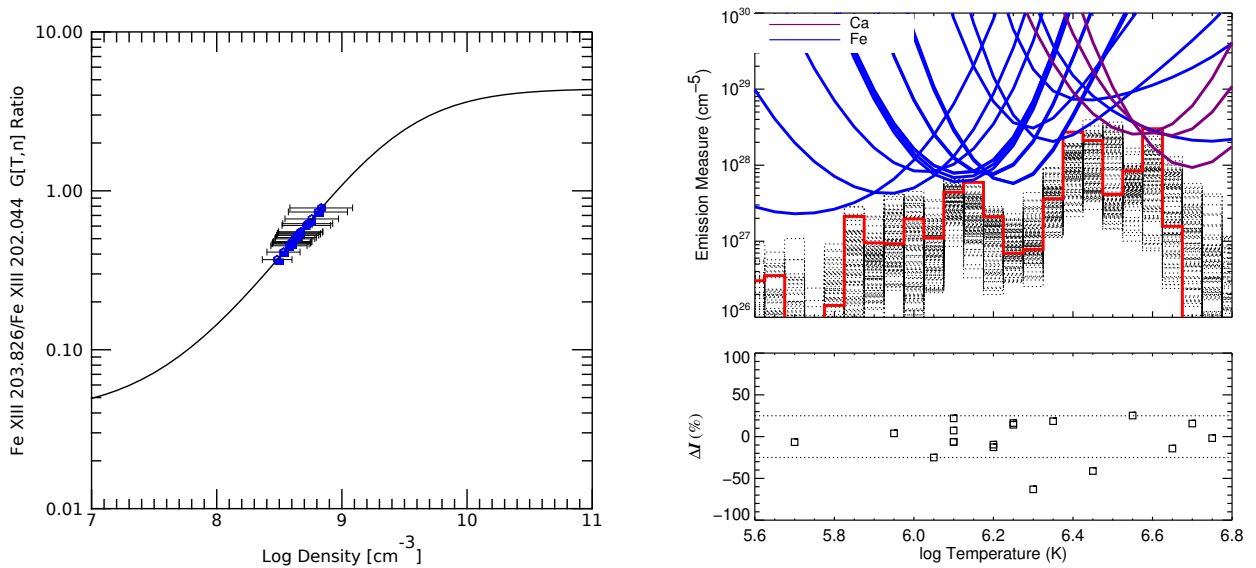
Figure 5. Cooling host loop coronal density and temperature analysis. Left panel: logarithmic electron density derived from the theoretical Fe XIII 203.826/202.044 line ratio. The ratio is shown by the solid black line. The blue dots indicate the measured densities within the dark blue boxes shown in Figure 2. The error bars show the range in densities that result from uncertainties in the observed ratio due to the radiometric calibration. Right panel (top): the emission measure (EM) distribution calculated from the Fe and Ca lines. The blue and magenta lines are EM loci curves that indicate the upper limits to the emission measure. The solid boxcar red line is the best fit solution from the MCMC algorithm. The dotted black lines show different realizations of the Monte Carlo solutions (see text). Right panel (bottom): differences between the observed and calculated intensities (expressed as a percentage) as a function of temperature. The dotted horizontal lines indicate an agreement level of 25%.

The density is a key quantity of interest. For the Fe XIII ratio, we are making a measurement around 1.7 MK, which is close to the expected peak temperature of 'warm' active region loops (Reale 2014). Such loops are observed in their cooling phase (Ugarte-Urra et al. 2009), and coronal rain forms within them if they reach a low enough temperature. Since the observations take place after the X2.1 flare, it is unclear whether we are observing loops cooling in the active region after the influence of the flare has ended, or actual post-flare loops. In either case, at these temperatures, we are measuring the densities in the host loop where the coronal rain later forms.

Warm loops have narrow temperature distributions (Warren et al. 2008), but it is clear that in these observations we are observing the emission from multiple different structures at different temperatures along the line-of-sight (coronal rain, warm loops, high-temperature loops). Initially, we therefore derive the DEM including all the spectral lines in our analysis. This is because we use this DEM primarily for measuring the elemental abundances. In section 3.5, we attempt to isolate the emission from the coronal rain itself.

Figure 5 (left panel) shows the theoretical Fe XIII 203.826/202.044 intensity ratio plotted against density, and the measurements in all the dark blue boxes as blue dots. Densities in the host loops fall in the range of $\log(n/cm^{-3}) = 8.5$–8.8, with a mean value of $\log(n/cm^{-3}) = 8.65$. We show an example of the emission measure (EM) distribution from one of the boxes in the right panel of Figure 5. The distribution covers a broad range of temperatures reflecting the fact that we are observing emission from the transition region and active region loops, all the way up to the high temperature active region or post-flare loops. The EM in this case peaks around 2.8 MK, and is well constrained by the high temperature Ca lines. A well-constrained EM at these temperatures is critical for the plasma composition measurements. The specific lines used, together with the observed and calculated intensities, and the percentage differences between them are shown in Table 1. The figure and table show that 16/18 (89%) of the line intensities are reproduced to within the EIS intensity calibration uncertainty of ∼23% (Lang et al. 2006).

3.4. *Plasma composition in the host loops*

To measure the plasma composition we compute the FIP bias (ratio of coronal to photospheric composition)

Table 1. EIS DEM analysis on 03-Mar-2023

ID	I_{obs}	I_{calc}	$\Delta[\%]$
Fe VIII 185.213	451.4±99.6	475.6	5.4
Fe IX 197.862	99.6±22.1	104.8	5.2
Fe X 184.536	846.6±186.7	727.0	-14.1
Fe XI 192.813	356.2±78.6	322.9	-9.3
Fe XI 180.401	3502.6±771.7	3166.3	-9.6
Fe XI 188.216	1304.3±287.2	1536.7	17.8
Fe XI 188.299	899.3±198.0	932.3	3.7
Fe XII 195.119	2302.6±506.7	1817.7	-21.1
Fe XII 192.394	712.8±156.9	583.0	-18.2
Fe XIII 203.826	750.5±167.2	875.6	16.7
Fe XIII 202.044	1127.9±248.6	1345.8	19.3
Fe XIV 264.787	2566.7±564.7	935.7	-63.5
Fe XV 284.160	10810.2±2378.3	12182.4	12.7
Fe XVI 262.984	1469.6±323.4	855.8	-41.8
Fe XVII 254.87	30.9±7.6	31.9	3.2
Ca XIV 193.874	97.4±21.6	118.8	22.1
Ca XV 200.972	76.8±17.7	60.2	-21.5
Ca XVI 208.604	24.3±16.9	29.6	22.1

EIS line intensities are in units of erg cm^{-2} s^{-1} steradian^{-1}.

by modeling two intensity ratios that are sensitive to the elemental abundances: Si X 258.375 Å/S X 264.223 Å, and Ca XIV 193.784 Å/Ar XIV 194.396 Å. The DEM is derived in each box using the method described in Section 3.3. Only lines from the low-FIP elements Fe and Ca are used in this analysis (see Table 1). The Ca lines are necessary to provide constraints on the DEM at the high temperatures where the Ca/Ar ratio is determined. Their impact on the DEM at the formation temperature of the Si/S ratio is less important. As discussed in Section 3.3, we assumed photospheric abundances when calculating the DEM. From here, the method to calculate the Si/S ratio is the same as we have used previously (Brooks & Warren 2011; Brooks et al. 2015). The DEM solution is adjusted to match the Si X 258.375 Å intensity. This takes account of potential cross-detector calibration issues resulting from the fact that most of the Fe lines used in the DEM analysis lie on the short-wavelength detector, whereas the Si and S lines lie on the long-wavelength detector. The S X 264.223 Å line intensity is then computed, and the ratio of the calculated to observed intensity is the FIP bias, $f_{Si/S}$. For the Ca/Ar ratio, no adjustment to the DEM is made because both the lines lie on the short-wavelength detector, and the DEM is already constrained by the Ca
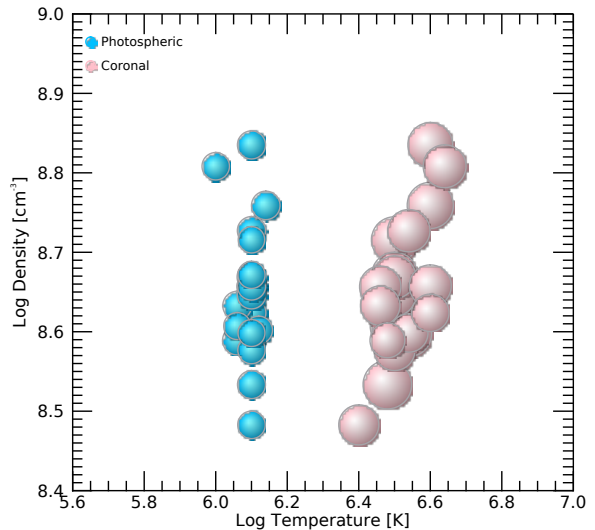

Figure 6. Cooling host loop coronal composition analysis. Bubble plot of the FIP bias factors measured in the dark blue boxes of Figure 2 using the Si/S and Ca/Ar abundance diagnostic ratios. The results are plotted at the electron density measured using Fe XIII and the effective formation temperature of S X 258.375 Å (log T ∼6.1) and Ca XIV 193.874 Å (log T ∼6.5). The size of the bubble is proportional to the magnitude of the FIP bias. Sky blue indicates that the FIP bias is photospheric (<1.5), and pink indicates that it is coronal (>1.5). The bifurcation at the two temperatures is evident.

lines. The ratio of the predicted and observed intensities of Ar XIV 194.396 Å yields the FIP bias, $f_{Ca/Ar}$. This method attempts to remove any diagnostic dependence on temperature and/or density. The Ca/Ar ratio has been used successfully for previous abundance measurements in flares (Doschek et al. 2015; Baker et al. 2019).

Figure 6 is a bubble plot showing the measured values of $f_{Si/S}$ and $f_{Ca/Ar}$ as a function of the electron density and effective formation temperature in each box. There is a clear difference in the distributions at the two formation temperatures. For Si/S (log T ∼6.1) the values fall in the range of $f_{Si/S}$ = 1.2–1.5, with a mean of $f_{Si/S}$ = 1.3, indicating photospheric abundances. For Ca/Ar (log T ∼6.5) the values fall in the range of $f_{Ca/Ar}$ = 2.0–4.0, with a mean of $f_{Ca/Ar}$ = 3.1, indicating coronal abundances.

Generally we have found that the scaling factor between Si and Fe can be up to a factor of 2. This contrasts with measurements earlier in the mission where the scaling was always less than the calibration uncertainty (see, e.g., Brooks & Warren 2011). It suggests there has been a change in the short- to long-wavelength calibration and

this is currently being assessed (Del Zanna et al. 2023). Our method corrects for any calibration evolution.

3.5. Coronal rain density and temperature analysis

The Mg VII 280.737/278.402 ratio provides a density measurement at around 0.8 MK, close to where the actual coronal rain is forming and is observable with EIS. A lower temperature constraint from Mg VI 270.394 Å, and surrounding temperature lines from Fe VIII upwards, allow us to attempt to isolate the DEM distribution for the coronal rain itself. Transition region emission is, however, weak in EIS observations and this complicates the analysis. The Mg VI 270.394 Å line, for example, is blended on the long-wavelength side with the stronger Fe XIV 270.519 Å line. Also, the Mg VII 280.737/278.402 ratio was discussed in application to transition region brightenings by Young et al. (2007) and they noted the presence of the Si VII 278.445 Å blend to Mg VII 278.402 Å. Fortunately, both these blends are easily separable with a double Gaussian fit. Young et al. (2007) also pointed out that the Mg VII 276.153 Å line could be used to give an independent check on the deblending of Mg VII 278.402 Å since the Mg VII 276.153/278.402 branching ratio has a fixed theoretical value. Unfortunately, this line is too weak in most of our boxes.

Figure 7 shows example line profiles for the weak Mg lines used in this analysis. The 3rd and 4th columns show the separation of the blended lines. In these columns, the Mg lines are the red curves and the blended lines are the light blue curves. The examples in this figure show where the limitations in the analysis are. As mentioned in Section 3.1, the most significant issue is the weak emission in Mg VII 280.737 Å. The figure contrasts a case where the Mg VII 280.737 Å emission in the box is weak, but is still strong enough that the spectral fit is acceptable (top row), with a case where the emission is too weak to get a good fit (bottom row). The figure also shows that the weakest Fe lines (Fe VIII 185.213 Å and Fe IX 197.862 Å) are strong enough that we can achieve a good fit in any box.

We found that an acceptable fit to the Mg VII 280.737 Å line was obtained in 12/20 dark blue boxes analyzed in the previous sections. To supplement these measurements we added 3 more boxes to bring the total number to 15. The additional boxes are shown in light blue in Figure 2 and Figure 8. Figure 8 (left panel) shows the theoretical Mg VII 280.737/278.402 intensity ratio plotted against density, the measurements in the 12/20 boxes where the fits were acceptable as blue dots, and the 3 supplementary boxes as light blue dots. Den-

sities in the coronal rain fall in the range of $\log(n/cm^{-3})$ = 9.1–9.9, with a mean value of $\log(n/cm^{-3}) = 9.35$.

The Mg VII 280.737 Å line is needed for the density measurement, but not for the DEM. For the DEM analysis, the weakest line is Mg VI 270.394 Å. Acceptable fits were obtained for this line in 18/20 dark blue boxes. From Figure 5 we can see that the EM distribution in the boxes is generally increasing with temperature, so the difficulty in isolating the coronal rain component is deciding where the cut-off should be between the rain and the host loop. For coronal loops, we would generally only include spectral lines that have highly correlated cross-field intensity profiles (see e.g. Aschwanden et al. 2008; Warren et al. 2008). This is not possible here, since the rain features are passing through the slit position and the boxes are too small for averaging along some spatial axis. Instead, we looked at the correlation between spectral line intensities in an area encompassing all the boxes along the coronal rain time-distance trails. Lines were included if the linear Pearson correlation with the Mg VII 280.737 Å area intensity was higher than $r = 0.6$. The intensities for the uncorrelated lines were set to zero, and the intensity error was set to 20% of the observed intensity. This is a fairly generous, low threshold that errs on the side of multi-thermality, however, the DEMs are narrow.

We show an example of the emission measure distribution from one of the boxes in the right panel of Figure 8. The EM peaks around 0.7 MK. Only the Mg VI 270.394 Å, Mg VII 280.737 Å, Fe VIII 185.213 Å, and Fe IX 197.862 Å lines meet the correlation threshold so the distribution is forced down rapidly at higher temperatures. In this example, all the observed intensities are reproduced to within 30%. The best-fit MCMC solution (thick red line) also shows that the EM distribution is narrow. We have overplotted a Gaussian fit with a width of $\sigma_T = 174,000$ K to the MCMC solution. This is narrower than most warm coronal loops (Warren et al. 2008), and the MCMC solution is narrower still.

3.6. Potential sources of non-thermal line broadening

In Section 3.2 we found an increase in non-thermal velocities with decreasing temperatures. This result could indicate the presence of turbulence, or it could result from pressure broadening or opacity broadening.

Following Milligan (2011), we can estimate the amount of pressure broadening from

$$\delta\lambda \sim \frac{\lambda^2}{c} \frac{n\sigma}{\pi} \sqrt{(2k_B T/M)} \qquad (2)$$

where λ is the wavelength of the spectral line, c is the speed of light, n is the electron density, σ is the colli-
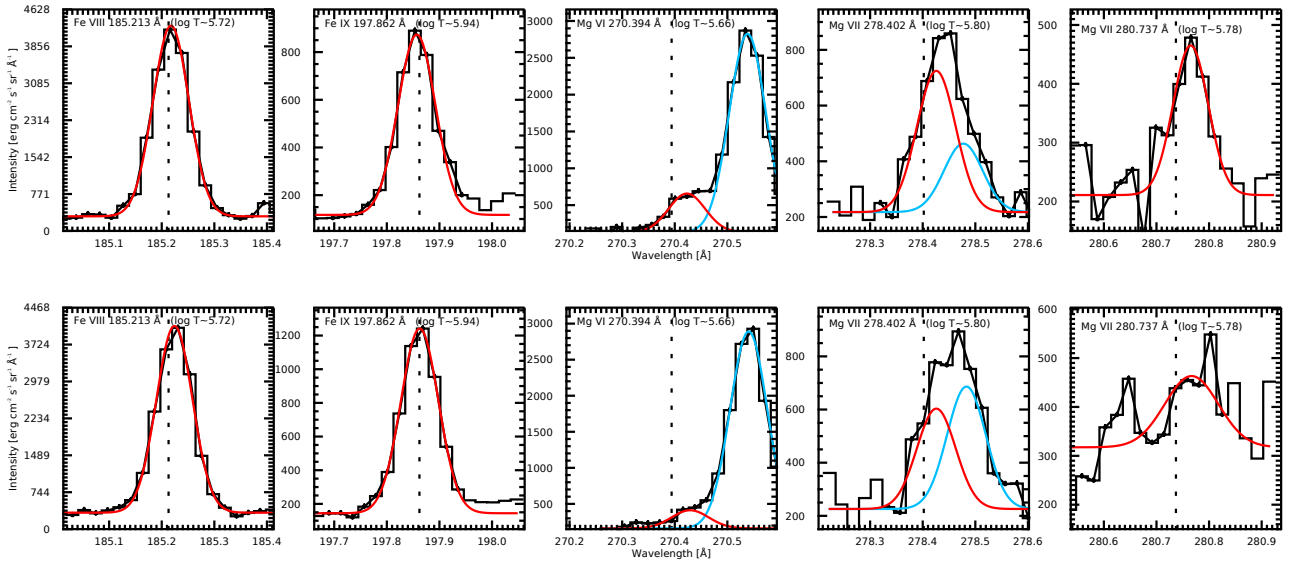
Figure 7. Example line profiles in the coronal rain showers. Top row: example box (from Figure 2) where the weakest line (Mg VII 280.737 Å) is still strong enough that we consider it well-fitted. The black histograms and small stars show the EIS data. The red lines show the Gaussian fits to the Fe and Mg lines of interest. The light blue lines show Gaussian fits to the blends i.e. in the 3rd column, Fe XIV 270.519 Å (light blue) blends with Mg VII 280.737 Å (red), and in the 4th column, Si VII 278.445 Å (light blue) blends with Mg VII 278.402 Å (red). The solid black curves show the composite fit from the main and blended lines. The Fe and Mg spectral lines are indicated in the legends along with their theoretical formation temperatures. The dotted vertical lines show the rest wavelength. Mg VII 278.402 Å and Mg VII 280.737 Å are the density diagnostic pair, and Mg VI 276.153 Å is the other Mg line used in the coronal rain emission measure analysis. Fe VIII 185.213 Å and Fe IX 197.862 Å are the weakest Fe lines used in our analysis, and they are plotted to show that they are strong enough to be well-fitted in all the blue boxes. Bottom row: example where Mg VII 280.737 Å has the lowest intensity of all the boxes and the fit is not good.

sional ionisation cross-section, T is the formation temperature, k_B is Boltzmann's constant, and M is the ion mass. Milligan (2011) showed that $\delta\lambda \sim 10^{-15}$ Å for the Fe XIV 264.787 Å and Fe XIV 274.203 Å lines used in his study of the hard X-ray footpoints of a solar flare and was therefore negligible. Milligan (2011) assumed a density of 10^{11} cm^{-3} for this calculation. Since $\delta\lambda$ depends linearly on density in Equation 2, we expect that the contribution from pressure broadening is even smaller for these lines in our host loops (mean $\log(n/cm^{-3})$=8.65 from the Fe XIII ratio - see Section 3.3). At the lowest temperatures where the non-thermal velocities were measured using Fe VIII 185.213 Å, the densities are higher (mean $\log(n/cm^{-3})$=9.35 from the Mg VII ratio - see Section 3.5), but are still over an order of magnitude lower than 10^{11} cm^{-3}. Some other factors in Equation 2 (λ, T, σ) do change, but their effect is to cancel each other: λ decreases from 264.787 Å to 185.213 Å, T decreases from 2 MK to 0.45 MK, and σ increases from e.g. 5 to 35 $\times 10^{-19}$ cm^{-2} at 1000 eV (Hahn et al. 2011, 2015). We conclude that pressure broadening does not impact our measurements.

The optical depth of a spectral line at line center can be expressed as given by Mitchell & Zemansky (1961),

$$\tau_0 = 1.16 \times 10^{-6} \sqrt{M/T}\lambda N_l f_{lu} h \qquad (3)$$

where f_{lu} is the absorption oscillator strength for the transition from the lower (l) to the upper (u) level, h is the path length, and N_l is the population of the lower level. Using oscillator strengths from the CHIANTI v.10 database, and adopting the coronal element abundances of Feldman (1992) together with the CHIANTI ionisation fractions (to calculate N_l), we computed values of τ_0 for Fe XIII 202.044 Å and Fe VIII 186.601 Å using the densities quoted above for the closest temperature. Both of these lines arise from transitions that terminate in the ground state of their respective ions (so N_l = the ground state). We assume a typical value of 300 km for the size of the coronal rain clump. We find that for Fe XIII 202.044 Å, $\tau_0 = 0.003$, and for Fe VIII 186.601 Å, $\tau_0 = 0.2$, indicating that both lines are optically thin and therefore opacity broadening is not significant.

Though it is unclear if we should expect the rain clumps to be more turbulent that the surrounding host loops, with pressure and opacity broadening ruled out, and lacking any other obvious explanations, we suggest
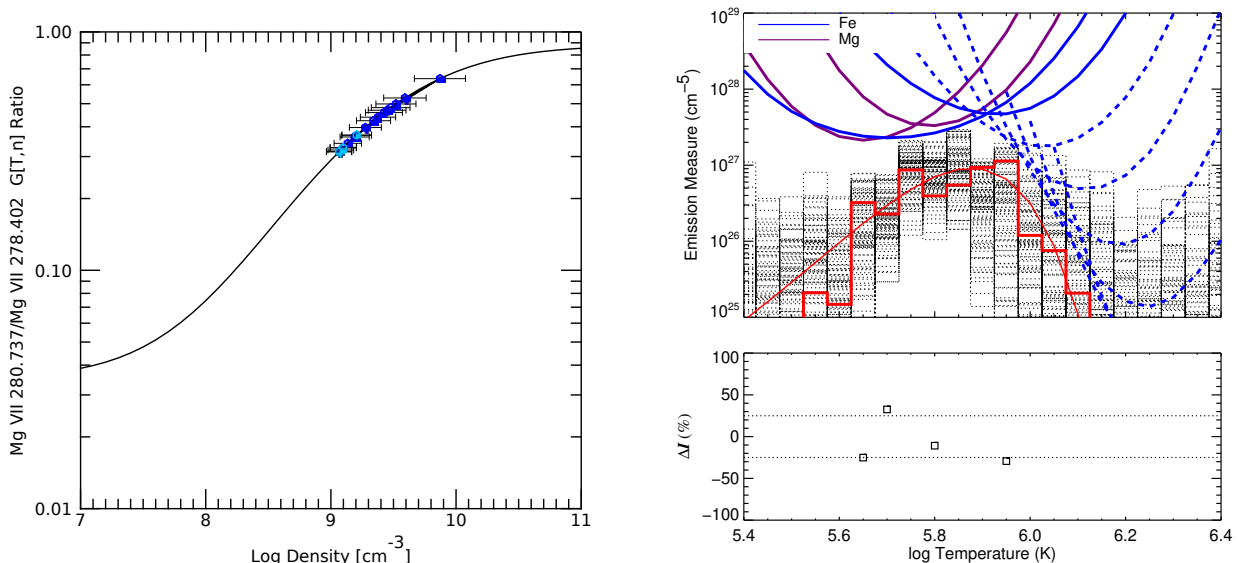
Figure 8. Coronal rain density and temperature analysis. Left panel: logarithmic electron density derived from the theoretical Mg VII 280.737/278.402 line ratio. The ratio is shown by the solid black line. The blue dots indicate the measured densities within 12/20 of the dark blue boxes shown in Figure 2 and the light blue dots show the densities measured in the light blue boxes in Figure 2 that were added to the analysis to obtain extra Mg VII 280.737 Å measurements with a good S/N. The error bars show the range in densities that results from uncertainties in the observed ratio due to the radiometric calibration. Right panel (top): the emission measure (EM) distribution calculated from the Mg and Fe lines where the intensity distributions are correlated with Mg VII 278.402 Å. The blue and magenta lines are EM loci curves that indicate the upper limits to the emission measure. The dashed lines are EM loci curves for lines where the intensity distributions are not correlated with Mg VII 278.402 Å. The solid boxcar red line is the best fit solution from the MCMC algorithm. The dotted black lines show different realizations of the Monte Carlo solutions). The smooth thin red line is a Gaussian fit to the MCMC solution with a width of $\sigma_T = 174,000$ K. Right panel (bottom): differences between the observed and calculated intensities (expressed as a percentage) as a function of temperature. The dotted horizontal lines indicate an agreement level of 25%.

that the broadening is a result of turbulence as the rain condensations form.

4. DISCUSSION AND CONCLUSIONS

We have applied several spectroscopic diagnostics to a rare set of EIS sit-and-stare observations of post-flare loop cooling and the formation and evolution of coronal rain showers, including when the rain is first condensing. The main observational results suggest the following picture. Quiescent coronal rain is present in the active region before the X2.1 flare. The flare, however, destabilizes and energises the loop arcade, and EIS observes while the loop system is relaxing to its pre-flare state. We observe a coronal composition in the high temperature (~ 3.5 MK) loops, that then cool down to ~ 1.3 MK, where we measure typical densities of $\log(n/cm^{-3}) \sim 8.65$. At these temperatures, the plasma composition is photospheric. As the loops cool further, coronal rain forms, with higher densities of $\log(n/cm^{-3}) \sim 9.35$ reached at 0.7 MK. Non-thermal velocities also increase as the temperature decreases. The temperature distributions in the rain showers are nar-

row. Coronal rain is visible throughout the observations, and is seen in loops disrupted by the flare close to the impulsive phase. These are important constraints for numerical modeling and understanding the formation of coronal rain.

The bifurcation in plasma composition measurements at the two temperatures does suggest we are observing post-flare driven coronal rain. In quiescent conditions, active region loops should show a coronal composition in both the Si/S and Ca/Ar diagnostic. Based on the ponderomotive force model of the FIP effect (Laming 2004, 2015), where the forces are induced by reflection and refraction of Alfvén waves generated by coronal (nanoflare) reconnection, low FIP (ionized) material is preferentially accelerated from the top of the chromosphere (Brooks & Yardley 2021), and this qualitatively reproduces the expected behavior of Si/S and Ca/Ar in AR loops. It is unclear by what process a coronal composition loop could develop a photospheric composition as it cools. In flaring conditions, however, the energy is sufficient to ablate plasma from the deep chromosphere. There S acts like a low-FIP element, so that it fraction-

ates in a similar manner to Si, and no FIP effect is detected in the Si/S ratio. The FIP effect is, however, still detected in Ca/Ar, and this naturally explains what we see here. This difference in Si/S and Ca/Ar is in effect a diagnostic of the source of the coronal plasma because S behaves differently depending on the fractionation location (Laming et al. 2019).

The increase in non-thermal velocities and densities with decreasing temperature suggests the development of turbulence as the coronal rain condensations form in the host loops. Our direct measurements of densities in the rain showers are somewhat lower than previously reported in the chromosphere. This is likely due to the uncertainties in inferring densities indirectly from imaging data, and also because we are making measurements early in the formation at higher temperatures. The densities are likely to grow as the instability and thermal runaway continues.

The transition to loop emission at the temperature of Fe X suggests rain should start to form $\sim 1.1\,\mathrm{MK}$. The formation of coronal rain is also influenced by the magnitude of the radiative losses, since they increase as the plasma cools, and these are affected by the plasma composition. In quiescent rain, the host loops have a coronal composition and typical radiative loss function with S behaving like a high-FIP element (S would behave this way even if the loops had a photospheric composition). In the flare-driven rain we observe here, however, once the host loops have cooled to around $1\,\mathrm{MK}$, the radiative losses are increased. This is because, as discussed above, S behaves like a low-FIP element and is enhanced in addition to all the other low FIP elements. The increased radiative losses thus make it easier for rain to form and cause it to cool more rapidly. This difference in radiative losses, driven by the behavior of S, is an essential difference between flare-driven and quiescent rain.

Coronal rain appears to show coherent behavior in imaging data, leading to the use of the term rain showers. The narrow temperature distributions measured by EIS in the rain showers support this idea of rain features evolving coherently. This is also reminiscent of the collective evolution of strands in the overlying coronal loops themselves (Warren et al. 2008), suggesting that rain showers might correspond to the host loops, and rain blobs might correspond to the loop threads. There

is some supporting evidence for this scenario from numerical simulations, which show that rain forms initially on one strand, but clearly occurs across multiple strands (Antolin et al. 2022; Li et al. 2022).

The spatio-temporal resolution of EIS is not sufficient to resolve either the 200-300 km average size of the rain blobs, or loop strands. Modeling of the cross-loop intensity profiles, however, suggests that a future instrument with a spatial resolution of 200 km should be able to resolve coronal loops (Brooks & Warren 2012; Brooks et al. 2013). This spatial resolution will be achieved by the Solar-C Extreme UltraViolet high-throughput Spectroscopic Telescope (EUVST, Shimizu et al. 2020). Our study shows the value of spectroscopic observations for gaining insights into properties of the heating mechanism from the loop cooling phase. The spatial resolution of Solar-C EUVST will be sufficient to resolve coronal loop threads and rain blobs, and the seamless broad temperature coverage will allow tracing of their evolution from the corona to the chromosphere.

Facilities: SDO/AIA, *Hinode*/EIS

REFERENCES

Ahn, K., Chae, J., Cho, K.-S., et al. 2014, SoPh, 289, 4117

Antiochos, S. K., MacNeice, P. J., Spicer, D. S., & Klimchuk, J. A. 1999, ApJ, 512, 985

Antolin, P. 2020, Plasma Physics and Controlled Fusion, 62, 014016

Antolin, P., & Froment, C. 2022, Frontiers in Astronomy and Space Sciences, 9, 820116

Antolin, P., Martínez-Sykora, J., & Şahin, S. 2022, ApJL, 926, L29

Antolin, P., & Rouppe van der Voort, L. 2012, ApJ, 745, 152

Antolin, P., Shibata, K., & Vissers, G. 2010, ApJ, 716, 154

Antolin, P., Vissers, G., Pereira, T. M. D., Rouppe van der Voort, L., & Scullion, E. 2015, ApJ, 806, 81

Aschwanden, M. J., Nitta, N. V., Wuelser, J.-P., & Lemen, J. R. 2008, ApJ, 680, 1477

Baker, D., van Driel-Gesztelyi, L., Brooks, D. H., et al. 2019, ApJ, 875, 35

Brooks, D. H., Ugarte-Urra, I., & Warren, H. P. 2015, Nature Communications, 6, 5947

Brooks, D. H., & Warren, H. P. 2011, ApJL, 727, L13

—. 2012, ApJL, 760, L5

—. 2016, ApJ, 820, 63

Brooks, D. H., Warren, H. P., Ugarte-Urra, I., & Winebarger, A. R. 2013, ApJL, 772, L19

Brooks, D. H., & Yardley, S. L. 2021, Science Advances, 7, eabf0068

Brooks, D. H., Winebarger, A. R., Savage, S., et al. 2020, ApJ, 894, 144

Şahin, S., & Antolin, P. 2022, ApJL, 931, L27

Culhane, J. L., Harra, L. K., James, A. M., et al. 2007, Sol. Phys., 243, 19

De Pontieu, B., McIntosh, S. W., Hansteen, V. H., & Schrijver, C. J. 2009, ApJL, 701, L1

De Pontieu, B., McIntosh, S. W., Carlsson, M., et al. 2011, Science, 331, 55

Del Zanna, G., Dere, K. P., Young, P. R., & Landi, E. 2021, ApJ, 909, 38

Del Zanna, G., Weberg, M., & Warren, H. P. 2023, arXiv e-prints, arXiv:2308.06609

Dere, K. P., Landi, E., Mason, H. E., Monsignori Fossi, B. C., & Young, P. R. 1997, A&AS, 125, 149

Doschek, G. A., Warren, H. P., & Feldman, U. 2015, ApJL, 808, L7

Downs, C., Lionello, R., Mikić, Z., Linker, J. A., & Velli, M. 2016, ApJ, 832, 180

Feldman, U. 1992, PhyS, 46, 202

Freeland, S. L., & Handy, B. N. 1998, SoPh, 182, 497

Froment, C., Antolin, P., Henriques, V. M. J., Kohutova, P., & Rouppe van der Voort, L. H. M. 2020, A&A, 633, A11

Froment, C., Auchère, F., Bocchialini, K., et al. 2015, ApJ, 807, 158

Froment, C., Auchère, F., Mikić, Z., et al. 2018, ApJ, 855, 52

Gold, T., & Hoyle, F. 1960, MNRAS, 120, 89

Hahn, M., Grieser, M., Krantz, C., et al. 2011, ApJ, 735, 105

Hahn, M., Becker, A., Bernhardt, D., et al. 2015, ApJ, 813, 16

Jing, J., Xu, Y., Cao, W., et al. 2016, Scientific Reports, 6, 24319

Kamio, S., Hara, H., Watanabe, T., Fredvik, T., & Hansteen, V. H. 2010, SoPh, 266, 209

Karpen, J. T., Antiochos, S. K., Hohensee, M., Klimchuk, J. A., & MacNeice, P. J. 2001, ApJL, 553, L85

Kashyap, V., & Drake, J. J. 1998, ApJ, 503, 450

—. 2000, Bulletin of the Astronomical Society of India, 28, 475

Kleint, L., Antolin, P., Tian, H., et al. 2014, ApJL, 789, L42

Klimchuk, J. A. 2006, SoPh, 234, 41

Kohutova, P., Antolin, P., Popovas, A., Szydlarski, M., & Hansteen, V. H. 2020, A&A, 639, A20

Kohutova, P., & Verwichte, E. 2016, ApJ, 827, 39

Kohutova, P., Verwichte, E., & Froment, C. 2019, A&A, 630, A123

Kosugi, T., Matsuzaki, K., Sakao, T., et al. 2007, Sol. Phys., 243, 3

Laming, J. M. 2004, ApJ, 614, 1063

—. 2015, Living Reviews in Solar Physics, 12, 2

Laming, J. M., Vourlidas, A., Korendyke, C., et al. 2019, ApJ, 879, 124

Lang, J., Kent, B. J., Paustian, W., et al. 2006, ApOpt, 45, 8689

Lemen, J. R., Title, A. M., Akin, D. J., et al. 2012, Sol. Phys., 275, 17

Li, X., Keppens, R., & Zhou, Y. 2022, ApJ, 926, 216

Milligan, R. O. 2011, ApJ, 740, 70

Mitchell, A. C. G., & Zemansky, M. W. 1961, Resonance Radiation and Excited Atoms, Cambridge University Press

Müller, D. A. N., De Groof, A., Hansteen, V. H., & Peter, H. 2005, A&A, 436, 1067

Müller, D. A. N., Hansteen, V. H., & Peter, H. 2003, A&A, 411, 605

Oliver, R., Soler, R., Terradas, J., Zaqarashvili, T. V., & Khodachenko, M. L. 2014, ApJ, 784, 21

Parker, E. N. 1983, ApJ, 264, 642

—. 1988, ApJ, 330, 474

Parnell, C. E., & De Moortel, I. 2012, Philosophical Transactions of the Royal Society of London Series A, 370, 3217

Pesnell, W. D., Thompson, B. J., & Chamberlin, P. C. 2012, Sol. Phys., 275, 3

Peter, H. 2001, A&A, 374, 1108

Pontin, D. I., & Priest, E. R. 2022, Living Reviews in Solar Physics, 19, 1

Reale, F. 2014, Living Reviews in Solar Physics, 11, 4

Reep, J. W., Antolin, P., & Bradshaw, S. J. 2020, ApJ, 890, 100

Scharmer, G. B., Narayan, G., Hillberg, T., et al. 2008, ApJL, 689, L69

Schrijver, C. J. 2001, SoPh, 198, 325

Scott, P., Asplund, M., Grevesse, N., Bergemann, M., & Sauval, A. J. 2015a, A&A, 573, A26

Scott, P., Grevesse, N., Asplund, M., et al. 2015b, A&A, 573, A25

Scullion, E., Rouppe van der Voort, L., Antolin, P., et al. 2016, ApJ, 833, 184

Shay, M. A., Drake, J. F., Rogers, B. N., & Denton, R. E. 2001, J. Geophys. Res., 106, 3759

Shimizu, T., Imada, S., Kawate, T., et al. 2020, in Society of Photo-Optical Instrumentation Engineers (SPIE) Conference Series, Vol. 11444, Space Telescopes and Instrumentation 2020: Ultraviolet to Gamma Ray, ed. J.-W. A. den Herder, S. Nikzad, & K. Nakazawa, 114440N

Ugarte-Urra, I., Warren, H. P., & Brooks, D. H. 2009, ApJ, 695, 642

van Ballegooijen, A. A., Asgari-Targhi, M., Cranmer, S. R., & DeLuca, E. E. 2011, ApJ, 736, 3

Warren, H. P. 2014, ApJL, 786, L2

Warren, H. P., Brooks, D. H., Doschek, G. A., & Feldman, U. 2016, ApJ, 824, 56

Warren, H. P., Ugarte-Urra, I., Doschek, G. A., Brooks, D. H., & Williams, D. R. 2008, ApJL, 686, L131

Warren, H. P., Ugarte-Urra, I., & Landi, E. 2014, ApJS, 213, 11

Warren, H. P., Ugarte-Urra, I., Young, P. R., & Stenborg, G. 2011, ApJ, 727, 58

Watanabe, K., Masuda, S., & Segawa, T. 2012, SoPh, 279, 317

Wedemeyer-Böhm, S., Scullion, E., Steiner, O., et al. 2012, Nature, 486, 505

Winebarger, A. R., & Warren, H. P. 2004, ApJL, 610, L129

Young, P. R., Del Zanna, G., Mason, H. E., et al. 2007, PASJ, 59, S727